crystals

MDPI

Communication

Growth Behaviors of Bubbles and Intermetallic Compounds in Solidifying Al-5 wt.% Mn Alloy

Shudong Huang [1] and Wenquan Lu [1,2,3,*]

[1] School of Materials Science and Engineering, Shanghai Jiao Tong University, Shanghai 200240, China; huangshudong520@sjtu.edu.cn
[2] State Key Laboratory of Advanced Special Steel, Shanghai University, Shanghai 200444, China
[3] Shanghai Jiao Tong University Sichuan Research Institute, Chengdu 610213, China
* Correspondence: flytsing1003@sjtu.edu.cn

Abstract: The growth behaviors of hydrogen bubbles and intermetallic compounds (IMCs) during solidification of an Al-5 wt.% Mn alloy was investigated by synchrotron radiography. Results show that bubble collapse can increase hydrogen concentration in nearby Al melt, thus facilitating the formation and growth of new bubbles. Under the interference of Al_6Mn IMCs, the growth method of an individual bubble is changed from a Gaussian distribution to a linear model. Al_6Mn crystal growth can be divided into three stages: first an isotropic spherical crystal appears, then it evolves into primary branches, and eventually forms an irregular octahedron.

Keywords: Al-Mn alloy; bubbles; intermetallic compounds; synchrotron radiography

Citation: Huang, S.; Lu, W. Growth Behaviors of Bubbles and Intermetallic Compounds in Solidifying Al-5 wt.% Mn Alloy. *Crystals* **2024**, *14*, 613. https://doi.org/10.3390/cryst14070613

Academic Editor: Marek Sroka

Received: 27 May 2024
Revised: 17 June 2024
Accepted: 23 June 2024
Published: 30 June 2024

1. Introduction

Al-Mn alloys have been widely used in the automobile and aerospace industries due to their excellent plasticity and corrosion resistance [1–3]. As a large number of intermetallic compounds (IMCs) can form during solidification of Al-Mn alloys, and the type, morphology and distribution of IMCs have an important effect on their performances, much work has focused on the formation and growth dynamic of IMCs [3–6]. For example, H.J. Kang et al. [1,4] found that the primary Al_6Mn IMCs transformed from solid polyhedra to hollow structures and subsequently to dendrites with increasing growth velocity, and this transition is a result of the competitive growth of different crystallographic planes. Z.W. Chen et al. [7] concluded that the Al_6Mn morphology successively exhibits a block-like, feather-like, snowflake-like, and lotus leaf-like phase with increasing Mn content in a suction casting Al-Mn alloy. For the formation of IMCs in other processes, using a quasi in situ observation method, Qiao et al. [8] found that the smaller θ-angle β-Sn grains show asymmetric Cu-Sn IMC growth due to the diffusion anisotropic of the Cu atom, while the larger ones exhibit symmetric growth during isothermal aging. Chen et al. [9] quantified three kinds of TiB_2 agglomerates in in situ Al/TiB_2 composites and revealed that these three agglomerates come from three different reactions. Anton et al. [10] investigated the growth behavior of α-Al(FeMnCr)Si IMCs in solidifying recycled Al alloys by micro-focus X-ray imaging technique, they demonstrated that surface oxides can act as nucleation sites for α-Al(FeMnCr)Si IMCs, and their crystal types mainly depend on the applied growth conditions. Obviously, the formation and morphological evolution of IMCs mainly depends on the metallurgical history and the alloy composition.

In addition to IMCs, the hydrogen bubble is another commonly observed phase in solidifying Al-Mn alloy [5,6]. As the hydrogen bubble can reduce the mechanical properties of aluminum castings, a considerable amount of effort has been made to reveal the bubble behaviors [5,6,11–19]. It was shown that the bubble exercises a crucial influence on the IMCs growth. For example, we found that Al_4Mn IMCs can appear in Al-10 wt.% Mn alloys during heating, which is closely related to concentration fluctuation of Mn solute caused by

the bubble coalescence [6]. Additionally, the bubble can accelerate the IMCs dissolution in heating Al-5 wt.% Mn alloy [5] and can block the growth of IMCs in solidifying Al-12 wt.% Ni alloy [15]. Although a great deal of effort has been made, the detailed morphological features and dynamic growth information of bubbles and IMCs in solidifying Al-Mn alloy is still unrevealed. Furthermore, the effect of IMCs on the bubble behavior remains to be not fully elucidated in solidifying Al-Mn alloy.

Synchrotron radiation X-ray is an electromagnetic radiation emitted by accelerating electrons moving along a curved orbit under the influence of an external magnetic field. It is characterized by high intensity, high collimation, high brightness, and continuous wavelength spectrum. These properties enable it to penetrate the metallic materials to observe the microstructure evolution during solidification [20].

In this work, we directly observed the bubbles and IMCs evolution during solidification of the Al-5 wt.% Mn alloy by synchrotron radiography. The growth mechanism of the bubbles and IMCs is clarified. The results would provide a theoretical guide for understanding the solidification microstructure formation of Al-Mn alloys.

2. Materials and Methods

Mixture of block-shaped pure Al (99.99%) and pure Mn (99.99%) was used to fabricate Al-5 wt.% Mn alloy in a vacuum induction furnace. Like the spray casting method, the mixture materials were placed in a quartz crucible with a nozzle (about 0.5 mm in diameter) at its bottom and were heated by induction melting under argon atmosphere. After the alloy melt was heated to a molten state and uniformly mixed, it was ejected from the nozzle into a Cu mold by high-pressure argon gas. Then, the prepared ingot was cut and polished to thin sheet with the size of 12 × 8 × 0.4 mm. There is a short distance between the quartz tube and the copper mold during the injection, leading to rapid cooling of the melt. Therefore, the copper impurities introduced during this process are negligible and primarily concentrated on the surface of the alloy, which are removed during subsequent machining steps. The detailed preparation process can also be found in our previous work [6].

The sliced Al-5 wt.% Mn alloy sample was enclosed between two aluminum oxide sheets and was overheated to 1118 K, which is much higher than its liquidus temperature according to the Al-Mn phase diagram [21], and can ensure sufficient mixing of components. Then, the overheated alloy melt cools by turning off the furnace with the cooling rate of 0.11 K/s, and the structural evolution during cooling was tracked by X-ray imaging experiments at BL13W1 beam line station of Shanghai Synchrotron Radiation Facility (SSRF). The samples were sandwiched between two thin alumina sheets for two reasons: (1) to keep the molten sample still on the X-ray path, preventing the Al-Mn alloy melt outflow from the view field; (2) as alumina has a low density and small X-ray absorption coefficient, it allows X-rays to pass through easily without significantly affecting imaging effect. The sketch of the imaging process can be found in ref. [6]. The X-ray energy, pixel size and exposure time we used are 26 keV, 3.25 μm and 1.5 s, respectively. The Crystallographic Information File (CIF file) of the Al_6Mn IMCs is obtained from the Materials Project database. All of the Al_6Mn crystal structure pictures are obtained by importing the CIF file of Al_6Mn into the Vesta software (Visualization for Electronic and Structural Analysis, Ver. 3.5.8).

3. Results and Discussion

3.1. Growth Behavior of Bubbles

Figure 1 shows the synchrotron images of microstructural evolution during solidification of the Al-5 wt.% Mn alloy. The light circle phase is the hydrogen bubble, the irregular gray phase is Al-Mn IMCs, which is identified as the Al_6Mn phase according to the Al-Mn alloy phase diagram [21] and Kang et al. [1,2]. The time when the Al-Mn alloy started to cool was set as the initial time (0 s). Three irregular shrinkage pores appear under high-temperature conditions (Figure 1a), and these three pores would come from the Al_2O_3 bi-film effect [22]. As seen in Figure 1, bubble 1# grows first (Figure 1b–e), then

breaks up (Figure 1e,f, the breaking up is visible in Figure 1f) and finally disappears at 666 s (Figure 1g). Bubble 2# appears at the position where bubble 1# had vanished and is fed by matrix liquid after the bubble collapse. With a continued decrease in temperature, Al_6Mn IMCs nucleate before 1036.5 s (Figure 1k), and the Al6Msn crystal grow in six different orientations [1,4]. Subsequently, bubble 3# nucleates, grows and deforms until it touches the growing Al_6Mn IMCs (Figure 1o,p) at 1842 s.

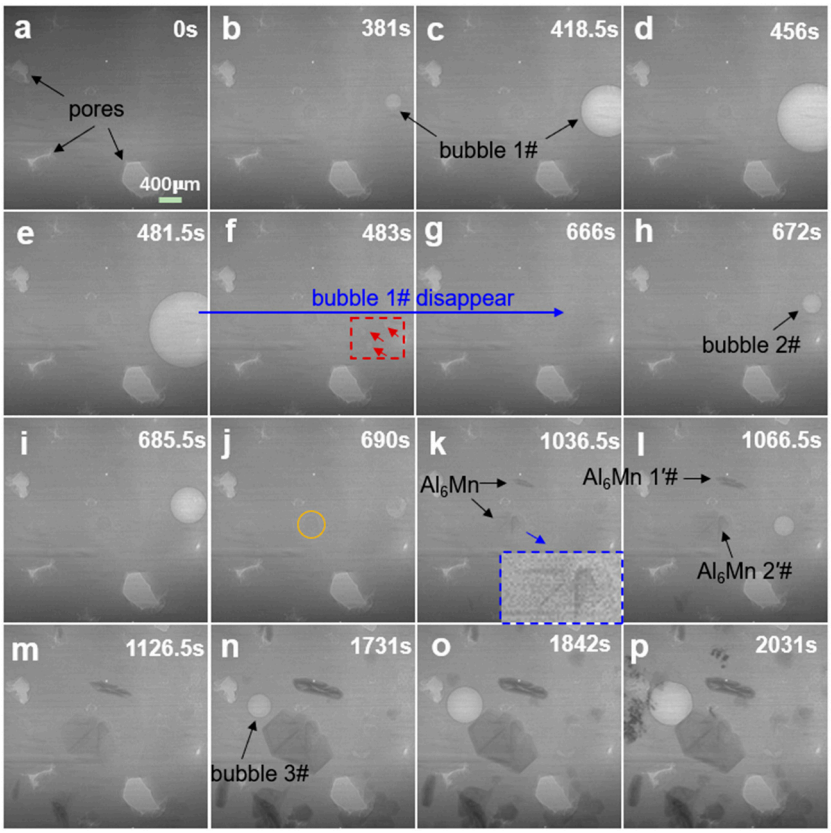

Figure 1. Synchrotron radiation images of the microstructure evolution during solidification of the Al-5 wt.% Mn alloy with the cooling rate of 0.11 K/s, the bubble appears light contrast, while the Al_6Mn IMCs exhibits dark gray, and the time when the Al-Mn alloy started to cool was set as 0 s.

Hydrogen in the Al-matrix melt mainly comes from the extensively reaction of water vapor with the molten Al [6,23,24]. The produced hydrogen atoms gathered around Al alloy surface and can dissolve into the molten Al. As the hydrogen solubility in solid Al is much smaller than that in liquid Al [15], hydrogen bubbles can easily form when hydrogen supersaturation builds up to the nucleation needed value during solidification. Therefore, most of the Al alloys have the bubble formation characteristic instead of only existing in the Al-Mn alloy.

For bubble 1#, the pressure inside the bubble (P_H) can be described as follows [16]:

$$P_H = P_{met} + \frac{2\gamma}{r} \quad (1)$$

where P_{met} is the metallostatic pressure, γ is the bubble/matrix melt interfacial energy, and r is the bubble radius. As the alloy viscosity increases with decreasing temperature, P_{met} will also increase. When $P_{met} + 2\gamma/r > P_H$, bubble 1# breaks into three small bubbles under the influence of metal static pressure (Figure 1e,f). Then, the three broken bubbles disappear with decreasing temperature (Figure 1g).

After that bubble 1# broken into three small bubbles for 186 s, bubble 2# appears in the same place as bubble #1 appeared (Figure 1h), which can be explained by the fluctuation of

hydrogen concentration in the Al melt. Whether the bubble forms or not mainly depends on the hydrogen concentration. When the hydrogen concentration reaches the critical supersaturation for nucleation, the bubble will nucleate [6,24]. In Figure 1, the collapse of bubble 1# can increase the hydrogen concentration and supersaturation in the nearby melt, facilitating the nucleation and growth of bubble 2#.

Figure 2 shows the time dependence of the bubble radius of the three marked bubbles in Figure 1. From Figure 2a, the Gaussian distribution can well describe the growth curve of bubble 1# and bubble 2#, which means that the bubble is dominated by hydrogen diffusion and grows in a stochastic way [18,19]. The sharp size reduction in bubble 2# is caused by the burst due to high internal pressure, then the Al-matrix melt feed at the position where bubble 2# collapsed (Figure 1j).

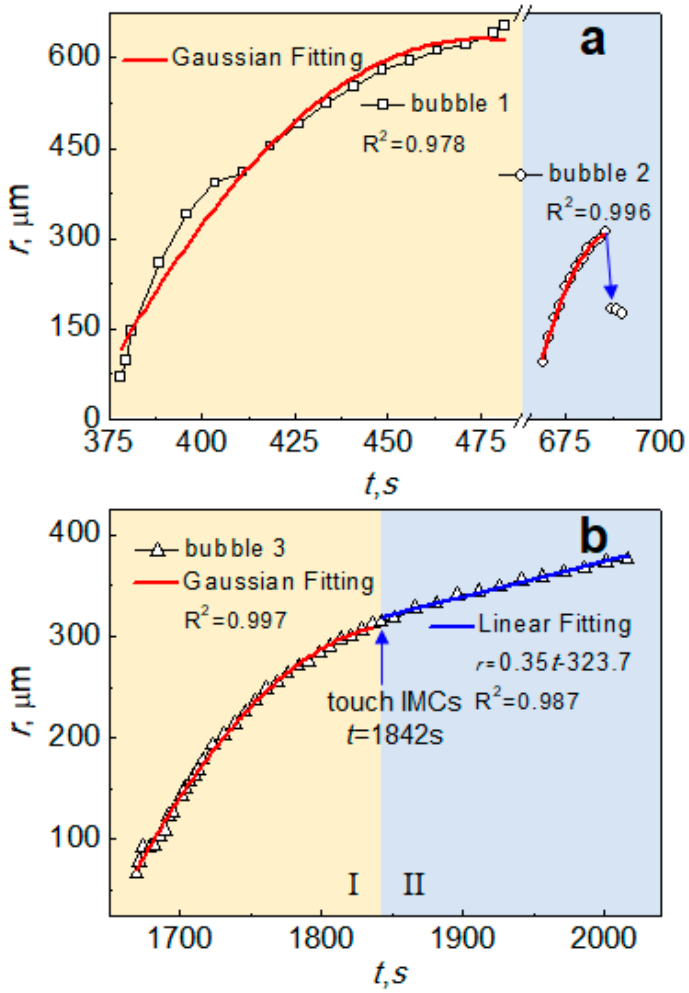

Figure 2. Variations of bubble radii with time for marked bubbles in Figure 1. (**a**) bubble 1# and bubble 2#; (**b**) bubble 3#.

From Figure 2b, the growth of bubble 3# can be divided into two stages. At stage I, as bubble 3# has not touched IMC, it can grow freely and follow Gaussian distribution [18,19]. At stage II, after the bubble 3# hit IMC at 1842 s, the bubble grows linearly with time. The main reason for this change is the variation in the hydrogen concentration gradient around the bubble. Figure 3 shows the hydrogen concentration distribution around the bubble. As shown in Figure 3a, the hydrogen concentration gradient shows a gradual decrease along the radial direction without the interference of surrounding IMCs. So, the growth rate gradually decreases with time at stage I.

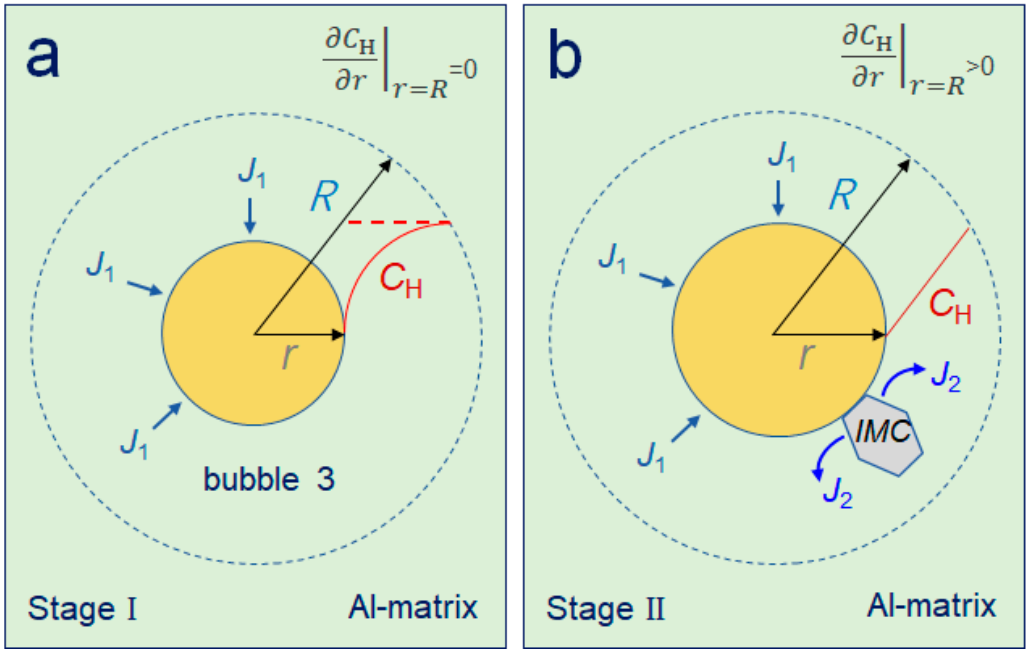

Figure 3. Variation of hydrogen concentration (C_H) in the surrounding melt of bubble 3#, J_1 the amount of hydrogen consumed by bubble growth, J_2 the amount of hydrogen released by IMCs growth. (**a**) the hydrogen concentration distribution around bubble 3# without the interference of surrounding IMC, (**b**) the hydrogen concentration distribution around bubble 3# with the interference of surrounding IMC.

After bubble 3# collided with the IMC (stage II), the bubble growth rate is almost constant (Figure 3b), which means the hydrogen concentration gradient around bubble 3# is a relatively stable value. This is mainly because the hydrogen solubility in the Al matrix melt is much larger than that in the Al_6Mn IMCs. The growth of Al_6Mn IMCs will consume the surrounding Al melt and thus release the hydrogen (the amount of hydrogen released is J_2 in Figure 3b), resulting in a considerable increase in hydrogen concentration around bubble 3#. Meanwhile, the growth of bubble 3# involves the consumption of hydrogen from the surrounding Al-Mn melt (the amount of hydrogen consumed is J_1 in Figure 3b), leading to a reduction in the hydrogen concentration in the matrix liquid. When the increase in hydrogen concentration in the nearby Al_6Mn melt equals to the decrease around the bubble 3# ($J_1 = J_2$), it will form a stable hydrogen concentration gradient around bubble 3#. This would explain why bubble 3# grows linearly at stage II.

3.2. Growth Mechanism of Al_6Mn IMCs

From Figure 1j–p, Al_6Mn IMCs gradually precipitate from the Al-matrix melt during solidification, and two IMCs, Al_6Mn 1′# and Al_6Mn 2′#, are almost simultaneously formed at 966 s. The surface oxide film of the aluminum melt (marked by orange circle in Figure 1j) acts as a heterogeneous nucleation site for Al_6Mn 2′# formation. Then, Al_6Mn 2′# grows along six different growth directions and presents a faceted growth characteristic (the larger version in Figure 1k,p).

Figure 4 shows the unit cell structure of Al_6Mn, and it has an orthorhombic structure with a = 6.38 Å, b = 7.46 Å, c = 8.76 Å, $\alpha = \beta = \gamma = 90^\circ$ [25]. From Figure 4, the closely packed Al atomic layers are approximately parallel to the (011) and (101) planes. As the growth rate of the closely packed crystal planes is slower than that of the loose ones, the close crystal faces are eventually preserved. Therefore, it tends to form an octahedron surrounded by eight closely packed (011) and (101) crystal faces under near equilibrium solidification conditions. Nevertheless, the final crystal shape should not be a regular octahedron because of the lattice constants a ≠ b ≠ c. By importing the Al_6Mn crystallographic information

in the Vesta software (Ver. 3.5.8), when the Al-Mn bond length increases from 2.7 Å to 4.2 Å, an irregular octahedron composed of six triangular faces and two quadrilateral faces appears (Figure 4e), and each Mn atom is surrounded by six Al atoms with the coordination number of 6. Therefore, six crystal faces can be observed from the top view of Al_6Mn 2′# in Figure 1m–p. When the bond distance further increases to 4.3 Å, an irregular tetrakaidecahedron appears with the coordination number of 10 (Figure 4f). According to Wang et al. [26], for cubic crystal, if V[100]/V[111] = $\sqrt{3}$ (V[100] and V[111] are the growth velocity along [100] and [111]), the crystal will grow into a perfect octahedral crystal; when V[100]/V[111] > $\sqrt{3}$, the crystal will grow in dendritic form; when V[100]/V[111] < $\sqrt{3}$, the crystal will grow into a tetrakaidecahedron [26]. So, it is a considerable possibility that tetrakaidecahedron and octahedral crystals can be formed during the actual growth process (Figure 4e,f).

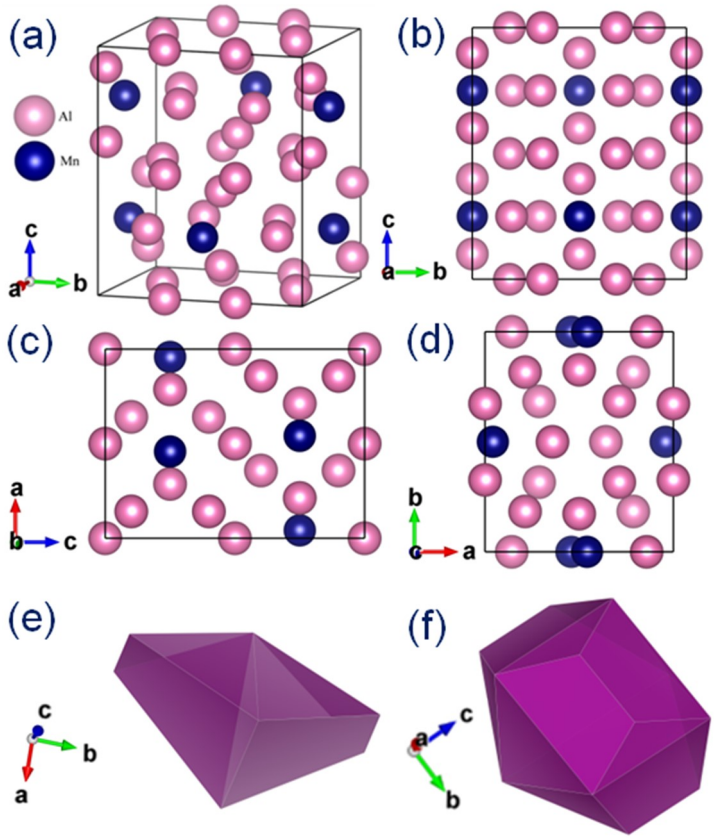

Figure 4. The unit cell of Al_6Mn intermetallic compound (**a**), the projections of Al_6Mn unit cell along the [100] (**b**), [010] (**c**) and [001] (**d**) directions, and sketch of Al_6Mn octahedron (**e**) and tetrakaidecahedron (**f**).

Figure 5a–c show the schematic of the Al_6Mn morphological evolution in solidifying the Al-Mn alloy. As the Al-Mn alloy was furnace-cooled under near equilibrium solidification conditions, the solute concentration gradient around the crystal embryo in the nearby matrix melt is symmetrical [27]. Therefore, the radial growth rate of the small embryo is isotropic, resulting in the formation of spherical crystal at the initial stage, as shown in Figure 5a,d. When the spherical crystal continues to grow and exceeds the critical size, it will gradually lose stability because of the difference in the packing density of different crystal faces [27]. The structural fluctuations on the crystal surface can lead to the formation of small hump, which will grow along the preferred growth direction (the most loosely packed direction <100>), and will evolve into primary branches (Figure 5b,e). Additionally, as the lattice parameter of orthogonal crystal is a ≠ b ≠ c, the growth rates in the six <100> directions are different, leading to faster growth in some directions than others (Figure 5e).

Further, compared with {100} crystal planes, {110} planes exhibit higher planar density and slower growth rates, therefore, the {100} crystal planes with high growth rates gradually shrink and disappear eventually. In contrast, the {110} crystal planes are preserved, leading to the formation of a standard octahedron.

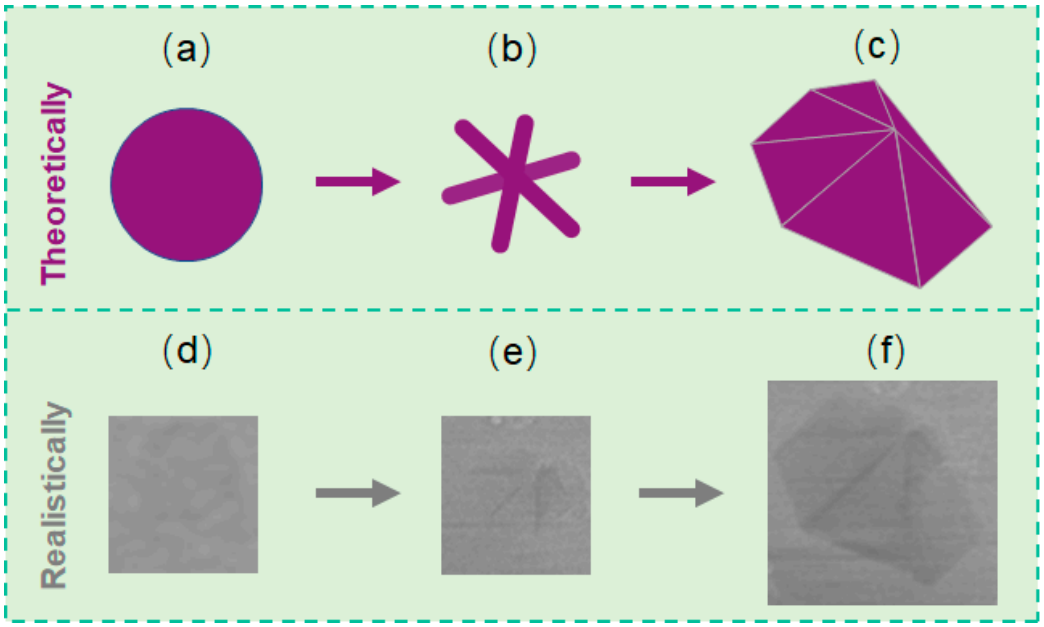

Figure 5. Three-dimensional morphology evolution of Al_6Mn IMC. (**a**,**d**) formation of an isotropic spherical crystal embryo at initial stage, (**b**,**e**) evolutionary branching at growth stage, and (**c**,**f**) irregular octahedron at final stage.

However, the real growth process of an orthogonal crystal is much more complex. When the lattice parameters or external environment (the solute and temperature fields) change, different polyhedra can be formed. As shown in Figure 5c, by adjusting the minimum bonding distance between Al and Mn in Vesta software, the irregular octahedron appears, which agrees well with the near-equilibrium solidification of Al_6Mn 2# (Figure 5f).

It should be noted that the formation of IMCs has a great effect on the mechanical properties of the alloy. The elongated polyhedral IMCs can result in severe concentration of stress, at which there is a great probability to cause crack formation and material fracture under the role of the external forces. Therefore, the elongated phase would cause harm to the mechanical properties of the Al-Mn alloy. On the contrary, if the IMCs are of near-spherical shapes and disperse uniformly in the Al-matrix, they would enhance the properties of the Al-Mn alloy because of second-phase strengthening. Additionally, static characterization methods, such as XRD and SEM, are used to indirectly study the phase structure and fracture morphology to reveal the fracture mechanism of the materials containing IMCs. Therefore, it is still not well understood how these fractures form. Our in situ synchrotron X-ray imaging studies of IMCs can effectively address this gap. By adjusting different solidification paths to control the morphological evolution of IMCs, we can understand the formation of the harmful second phase and propose an appropriate solidification condition that can obtain a fine and uniform structure.

4. Conclusions

In summary, the morphological evolution of hydrogen bubbles and IMCs in solidifying Al-5 wt.% Mn alloy has been investigated using the synchrotron X-ray imaging technique. Before touching Al_6Mn IMCs, the growth behavior of individual bubble follows a Gaussian distribution, then it grows linearly after contacting IMCs. Al_6Mn crystal growth goes through three phases: formation of an isotropic spherical crystal, evolutionary branching, and subsequent growth of an irregular octahedron.

Author Contributions: Conceptualization, W.L.; methodology, S.H. and W.L.; software, S.H. and W.L.; validation, S.H. and W.L.; formal analysis, S.H. and W.L.; investigation, S.H. and W.L.; resources, W.L.; data curation, S.H. and W.L.; writing—original draft preparation, S.H. and W.L.; writing—review and editing, W.L.; visualization, S.H. and W.L.; supervision, W.L.; project administration, W.L.; funding acquisition, W.L. All authors have read and agreed to the published version of the manuscript.

Funding: This work was funded by the Sichuan Science and Technology Program (No. 2022NSFSC1978) and the Open Project of State Key Laboratory of Advanced Special Steel, Shanghai Key Laboratory of Advanced Ferrometallurgy, Shanghai University (SKLASS 2022-09) and the Science and Technology Commission of Shanghai Municipality (No. 19DZ2270200).

Data Availability Statement: The data presented in this study are available on request from the corresponding author.

Acknowledgments: We appreciate Naifang Zhang and the staff members of the BL13W1 beam line of Shanghai Synchrotron Radiation Facility (SSRF) for their help with synchrotron experiments.

Conflicts of Interest: The authors declare no conflicts of interest.

References

1. Kang, H.; Li, J.; Wang, T.; Guo, J. Growth Behavior of Primary Intermetallic Phases and Mechanical Properties for Directionally Solidified Al-Mn-Be Alloy. *Acta Metall. Sin.* **2018**, *54*, 809–823.
2. Kang, H.; Li, X.; Su, Y.; Liu, D.; Guo, J.; Fu, H. 3-D Morphology and Growth Mechanism of Primary Al6Mn Intermetallic Compound in Directionally Solidified Al-3 at.% Mn Alloy. *Intermetallics* **2012**, *23*, 32–38. [CrossRef]
3. Bouché, K.; Barbier, F.; Coulet, A. Intermetallic Compound Layer Growth between Solid Iron and Molten Aluminium. *Mater. Sci. Eng. A* **1998**, *249*, 167–175. [CrossRef]
4. Kang, H.; Wang, T.; Li, X.; Su, Y.; Guo, J.; Fu, H. Faceted–Nonfaceted Growth Transition and 3-D Morphological Evolution of Primary Al_6Mn Microcrystals in Directionally Solidified Al–3 at.% Mn Alloy. *J. Mater. Res.* **2014**, *29*, 1256–1263. [CrossRef]
5. Lu, W.; Zhang, N.; Ren, N.; Ding, Z.; Yang, F.; Hu, Q.; Li, J. Bubble-Induced Formation of New Intermetallic Compounds in an Al-Mn Alloy during Heating Observed by Synchrotron Radiography. *Materialia* **2021**, *15*, 100991. [CrossRef]
6. Lu, W.; Zhang, N.; Ding, Z.; Yang, F.; Hu, Q.; Zeng, L.; Li, J. Bubble Growth, Intermetallic Compounds Dissolution and Their Interactions during Heating of an Al-5 wt.% Mn Alloy by in-Situ Synchrotron Radiography. *J. Alloys Compd.* **2020**, *822*, 153554. [CrossRef]
7. Chen, Z.; Hou, Y.; Xie, B.; Zhang, Q. Dendrite Morphology Evolution of Al_6Mn Phase in Suction Casting Al–Mn Alloys. *Materials* **2020**, *13*, 2388. [CrossRef]
8. Qiao, Y.; Ma, H.; Yu, F.; Zhao, N. Quasi-in-Situ Observation on Diffusion Anisotropy Dominated Asymmetrical Growth of Cu-Sn IMCs under Temperature Gradient. *Acta Mater.* **2021**, *217*, 117168. [CrossRef]
9. Chen, F.; Mao, F.; Chen, Z.; Han, J.; Yan, G.; Wang, T.; Cao, Z. Application of Synchrotron Radiation X-Ray Computed Tomography to Investigate the Agglomerating Behavior of TiB_2 Particles in Aluminum. *J. Alloys Compd.* **2015**, *622*, 831–836. [CrossRef]
10. Bjurenstedt, A.; Casari, D.; Seifeddine, S.; Mathiesen, R.H.; Dahle, A.K. In-Situ Study of Morphology and Growth of Primary α-Al(FeMnCr)Si Intermetallics in an Al-Si Alloy. *Acta Mater.* **2017**, *130*, 1–9. [CrossRef]
11. Bhagavath, S.; Gong, Z.; Wigger, T.; Shah, S.; Ghaffari, B.; Li, M.; Marathe, S.; Karagadde, S.; Lee, P. Mechanisms of gas and shrinkage porosity formation in solidifying shear bands. *J. Mater. Process. Technol.* **2022**, *299*, 117338. [CrossRef]
12. Li, X.; Yang, X.; Xue, C.; Wang, S.; Zhang, Y.; Wang, B.; Wang, J.; Lee, P. Predicting hydrogen microporosity in long solidification range ternary Al-Cu-Li alloys by coupling CALPHAD and cellular automata model. *Comp. Mater. Sci.* **2023**, *222*, 112120. [CrossRef]
13. Zhang, Q.; Sun, D.; Pan, S.; Zhu, M. Microporosity formation and dendrite growth during solidification of aluminum alloys: Modeling and experiment. *Int. J. Heat Mass Transf.* **2020**, *146*, 118838. [CrossRef]
14. Wang, J.; Li, M.; Allison, J.; Lee, P.D. Multiscale Modeling of the Influence of Fe Content in a Al–Si–Cu Alloy on the Size Distribution of Intermetallic Phases and Micropores. *J. Appl. Phys.* **2010**, *107*, 61804. [CrossRef]
15. Atwood, R.C.; Sridhar, S.; Zhang, W.; Lee, P.D. Diffusion-Controlled Growth of Hydrogen Pores in Aluminium–Silicon Castings: In Situ Observation and Modelling. *Acta Mater.* **2000**, *48*, 405–417. [CrossRef]
16. Lee, P.D.; Chirazi, A.; See, D. Modeling Microporosity in Aluminum–Silicon Alloys: A Review. *J. Light Met.* **2001**, *1*, 15–30. [CrossRef]
17. Zhang, Q.; Sun, D.; Zhang, S.; Wang, H.; Zhu, M. Modeling of microporosity formation and hydrogen concentration evolution during solidification of an Al–Si alloy. *Chin. Phys. B* **2020**, *29*, 78104. [CrossRef]
18. Sun, S.; Hu, Q.; Lu, W.; Ding, Z.; Xia, M.; Li, J. In Situ Observation on Bubble Behavior of Solidifying Al-Ni Alloy Under the Interference of Intermetallic Compounds. *Metall. Mater. Trans. A* **2018**, *49*, 4429–4434. [CrossRef]
19. Bhagavath, S.; Cai, B.; Atwood, R.; Li, M.; Ghaffari, B.; Lee, P.; Karagadde, S. Combined Deformation and Solidification-Driven Porosity Formation in Aluminum Alloys. *Metall. Mater. Trans. A* **2019**, *50*, 4891–4899. [CrossRef]

20. Chen, R.; Liu, P.; Xiao, T.; Xu, L.X. X-Ray Imaging for Non-Destructive Microstructure Analysis at SSRF. *Adv. Mater.* **2014**, *26*, 7688–7691. [CrossRef]
21. Liu, X.J.; Ohnuma, I.; Kainuma, R.; Ishida, K. Thermodynamic Assessment of the Aluminum-Manganese (Al-Mn) Binary Phase Diagram. *J. Phase Equilibria* **1999**, *20*, 45–56. [CrossRef]
22. Cao, X.; Campbell, J. The Nucleation of Fe-Rich Phases on Oxide Films in Al-11.5Si-0.4Mg Cast Alloys. *Met. Mater. Trans. A* **2003**, *34*, 1409–1420. [CrossRef]
23. Li, X.; Meng, Y.; Yang, X.; Xue, C.; Miao, Y.; Li, Q.; Hou, Q.; Li, Z.; Wang, J. Tracking Hydrogen Microporosity Evolution During Solidification of Al–Cu–Li Alloy Using Multiscale Model and Synchrotron Radiation X-ray Radiography. *Met. Mater. Trans. A* **2024**, *55*, 2428–2444. [CrossRef]
24. Lu, W.; Zhang, S.; Zhang, W.; Li, J. Imaging of Structure Evolution in Solidifying Al–Bi Immiscible Alloys by Synchrotron Radiography. *J. Mater. Sci. Technol.* **2016**, *32*, 1321–1325. [CrossRef]
25. Stenberg, L.; Sjövall, R.; Lidin, S. On the Compound Coordination Polyhedron in $MnAl_6$ and Fe_2Al_5. *J. Solid State Chem.* **1996**, *124*, 65–68. [CrossRef]
26. Wang, R.Y.; Lu, W.H.; Hogan, L.M. Faceted Growth of Silicon Crystals in Al-Si Alloys. *Metall. Mater. Trans. A* **1997**, *28*, 1233–1243. [CrossRef]
27. Li, C.; Wu, Y.Y.; Li, H.; Liu, X.F. Morphological Evolution and Growth Mechanism of Primary Mg_2Si Phase in Al–Mg2Si Alloys. *Acta Mater.* **2011**, *59*, 1058–1067. [CrossRef]